Electrodynamic enhancement of film cooling of turbine blades

Chin-Cheng Wang and Subrata Roy[a)]
Computational Plasma Dynamics Laboratory and Test Facility, Department of Mechanical and Aerospace Engineering, University of Florida, Gainesville, Florida 32611, USA

(Received 4 June 2008; accepted 12 August 2008; published online 7 October 2008)

Three concepts are numerically investigated to promote lateral mixing of the cold jets and to ensure their better attachment to the surface. First, we introduce electrodynamically enhanced interaction of cool air jets with hot crossflow for improved cooling of hot surfaces. We identify mechanisms to "push" or "pull" the essentially stagnant fluid just downstream of the hole by enforcing an active pressure pulsation in streamwise and crosswise directions. Such method utilizes electrodynamic force that induces attachment of cold jet to the work surface by actively altering the body force in the vicinity using a plasma actuator for different cooling hole geometries. Second, we employ a negative pressure region just downstream of the cooling hole. This may be generated by utilizing a suction vent or other mechanisms. Third, we propose three geometric modifications of the cooling hole exit for enhancing lateral tripping of the cold jet. Detailed computation of a single row of 35 degree round holes on a flat plate has been obtained for a select blowing ratio of 1.0 with a density ratio of 2.0. Results are compared with the published experimental results and other numerical predictions for the latest film cooling technology to identify effectiveness improvement. We have shown that a combination of plasma and geometric change can significantly improve the film cooling performance. © *2008 American Institute of Physics*. [DOI: 10.1063/1.2990074]

I. INTRODUCTION

Cooling of hot surfaces with cold fluid film is commonplace in many engineering problems. For example, gas turbines require proper cooling mechanism to protect its blades from thermal stresses due to hot combustion gases. The problem becomes aggravated by the need for higher turbine inlet temperature to generate more power. Film cooling is used as a mechanism for reducing such thermal stress and for increasing lifetime for a turbine blade. It works in the form of a row of holes located in the spanwise direction through which cold jets are issued into the hot crossflow. The penetration of a cold jet into the main flow creates a three-dimensional (3D) flow field. Thus, the trajectory and the physical path of a thermal jet and the mixing mechanism of jet in the crossflow are critical design parameters. Figure 1(a) shows the schematic of a single round jet injected in the crossflow at an angle. This geometry has been extensively investigated for cooling performance for a wide range of blowing ratio (i.e., momentum ratio of injected air to crossflow).

A summary of basic investigations of isothermal and thermal jets into crossflow is given in our prior publication.[1,2] These results show details of the vortex interaction region and mixing in the near and far field. Despite various innovative techniques,[3,4] the film cooling effectiveness is ultimately limited by the loss of flow attachment just downstream of the hole. This is due to the "lift-off" of the cold jet beyond a threshold momentum ratio. The film cooling configuration which is designed for peak flow performance may not actively regulate itself for off-design conditions. As a viable alternative, in this paper we introduce three possible designs of film cooling flow for the 3D geometry shown in Fig. 1. We explore ways to electrodynamically enhanced interaction of cool air jets with hot crossflow for improved cooling of hot surfaces.

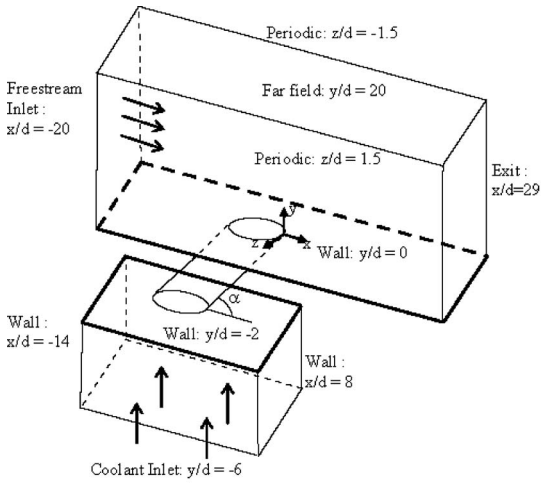

(a) Film cooling simulation geometry

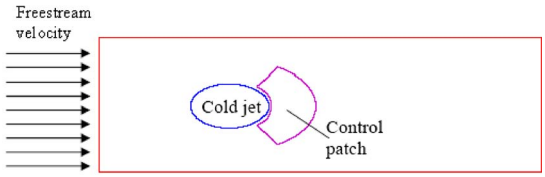

(b)Adiabatic flat plate with control patch

FIG. 1. (Color online) Schematic shows the film cooling flow. The geometry and boundary conditions are based on reported test setup (Refs. 6 and 8).

[a)]Author to whom correspondence should be addressed. Electronic mail: roy@ufl.edu.

An important parameter for comparing film cooling performance is its effectiveness $\eta=(T_{fs}-T_s)/(T_{fs}-T_j)$, where T_s, T_j, and T_{fs} are the work surface, cooling jet, and hot freestream gas temperatures, respectively. The effectiveness is plotted against a nondimensional ratio x/Md, where x is the downstream distance, $M=\rho_j u_j/\rho_f u_f$ is the blowing ratio, and d is the effective hole diameter. The density ρ_j and velocity u_j of the fluid at the jet exit plane are related to the freestream density ρ_f and velocity u_f such that $\rho_j/\rho_f=\mathrm{Mu}_f/u_j$. As compared to the slots, a row of discrete holes typically has a much lower span averaged downstream film effectiveness distribution for the same x/Md $(=x/d$ for $M=1)$ due to the formation of vortices which allow hot gas to penetrate to the wall. These vortices are of the scale of the hole size and smaller. It is essential for a computational mesh to have a minimum node spacing much smaller than the film hole spanwise pitch. Otherwise, such calculation becomes two dimensional on the scale of the film holes. Several experimental efforts[4–6] have been documented in the literature. They measured the scaling effect of the hole spacing to diameter ratio and the influence of the inclination of the holes to the surface on a flat plate and on curved (turbine blade-like) surfaces at different flow thermal conditions. Bunker[7] also provided a review of the shaped holes for film cooling. He summarized the benefits of shaped hole such as higher centerline and spanwise effectiveness than round hole and found little variation in effectiveness over blowing ratio from 0.5 to 2.

Numerical solutions of the full Navier–Stokes equations have also been used to obtain detailed solutions in various studies.[1,2,8–12] These efforts include closure models based on constant turbulent viscosity, variants of Reynolds averaged Navier–Stokes (RaNS), large eddy simulation (LES), and hybrid turbulence models (like DES). Numerical solutions for these flow arrangements document strong to moderate secondary vortex structures spanning normal to the direction of the jet. This fully 3D flow field strongly influences the cooling performance of the hole-blade system. Computational results predict an optimum hole spacing and low issuing angle for maximum cooling efficiency (for example, see Ref. 1).

Several computational studies have computed turbine blade geometries with accurate resolution of the film holes, and in some cases, of the hole pipes and plena as well. Garg and Rigby[10] resolved the plenum and hole pipes for a three-row showerhead film cooling arrangement with Wilcox's k-ω turbulence model, and Heidmann *et al.*[11] used RaNS to compute the heat transfer for a realistic turbine vane with 12 rows of film cooling holes with shaped holes and plena resolved. Garg[12] presented results of a full rotating blade with 172 film holes, resolving the cooling hole exits, but not the hole pipes and the plenum. These studies provide good details of the flow. However, the anisotropic dynamic nature of the spanwise vortices that affect the film cooling process are more complex than that can be captured by the mixing models used in aforementioned papers. The two competing factors important for any turbulence model are accuracy and efficiency (i.e., computational cost). An optimal combination of both these factors is hard to achieve and thus, the primary purpose of the numerical simulation is toward attaining such a goal. Although LES requires less computational effort or can simulate flows at higher Reynolds number than direct numerical simulation, one major challenge for performing LES in film cooling is the range of length scales that must be resolved in the computation (Lesieur *et al.*[13]).

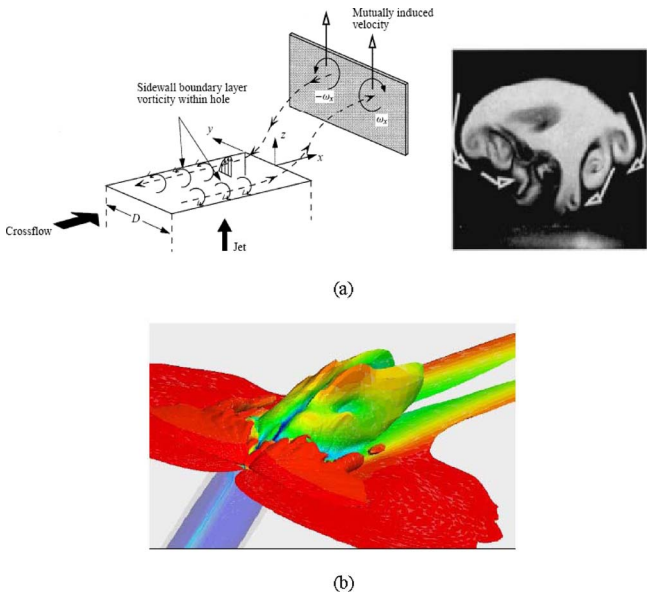

FIG. 2. (Color online) The penetration of the cold jet into the hot crossflow is a 3D process. (a) Flow interaction schematic (left) and LIF image (right) from Haven and Kurosaka (Ref. 15). (b) DES simulation from Kapadia *et al.* (Ref. 2).

As a remedy, Kapadia *et al.*[2] utilized a detached eddy simulation (DES) turbulence model[14] on a widely published blade-pipe configuration shown in Fig. 1(a) for a unit blowing ratio $(M=1)$. DES model makes no such assumption of isotropy downstream of the hole. Results indicate that the mixing processes downstream of the hole are highly anisotropic, as the turbulent diffusion is much stronger in the transverse direction. In comparison to the RaNS solution temperature distribution on the blade and near the vertical symmetry plane, DES captured better description of the dynamic flow structures.

In the near field of the film cooling jet, the dynamic large scale structures control the mixing process.[2,15] Such 3D mixing shown in Fig. 2 determines the normal and transverse penetration of the jet. Specifically, in Fig. 2(a) a schematic of a jet-crossflow interaction and a laser-induced fluorescence (LIF) image description are given from Haven and Kurosaka.[15] Figure 2(b) shows similar complex vertical structure from high-fidelity hybrid DES simulation of Kapadia *et al.*[2] We conjecture that accurate actuation of such flow field will greatly influence the near wall heat transfer process and the film cooling effectiveness. The complex dynamic nature of the spanwise vortices makes it necessary to use active mode of control that will interact with the flow field temporally and spatially in the near wall region. We will utilize the surface region denoted as the "control patch" (CP) in Fig. 1(b) for actively controlling the coolant flow and its 3D spread over the work surface.

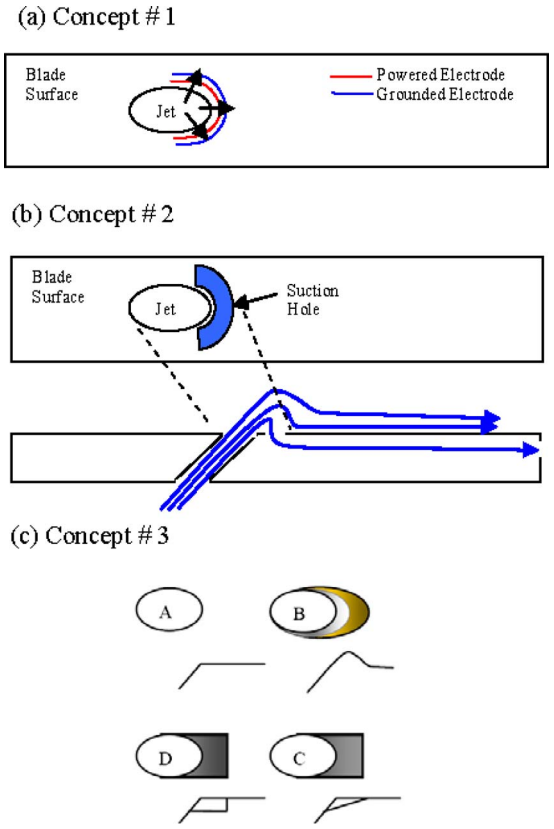

FIG. 3. (Color online) Design modifications for improved cooling.

II. DESIGN CONCEPTS

We introduce the following three design concepts as described in Fig. 3. Let us consider the first concept shown in Fig. 3(a). Here we use plasma actuator at the downstream (or upstream) of the cooling hole. Such actuators are made of a set of electrode pairs between which electric potential and induced weak ionization of the working gas generate an electric body force that is dominant inside the boundary layer. In such an actuator the flow actuation is directly linked with the gas-charged particle interaction and thus instantaneous.[16] A response pressure fluctuation occurs in the boundary layer gas interacting with the plasma due to fast plasma thermalization. A small fraction of power (less than 1% of the turbine power) will be utilized for such arrangement which may eventually reduce the energy budget by more effective cooling.

In the second configuration [Fig. 3(b)] a suction pressure is used just downstream of the cooling jet hole. The idea is to utilize the trail end pressure drop to attach the cool jet to the surface. Based on the blowing ratio, the pressure drop is going to vary across the blade chord. The dissimilarity in the shape and size of the cool jet and the suction holes may help in the three dimensional mixing. If hot gas entrainment is a concern, we can use the suction holes of equal or smaller size than the cool jet. The advantages include 3D dispersion of the cold jet without any major loss in flow energy. If cold gas is ingested, it will give an additional benefit due to cooling of the metal from the underside surface. It might be helpful to give the amount of fluid ingested for each back pressure to give an idea of the sensitivity. It is worth noting that there are similar concepts for suction aided film cooling,[17–19] however, they are distinctly different than the present design due to the location and configuration of the proposed suction hole.

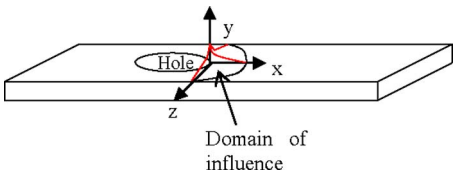

FIG. 4. (Color online) Force model used to approximate a plasma actuator.

The third concept is to utilize alternate designs of the cooling hole exit. Figure 3(c) shows schematics of various shapes of the hole exit plane: A is the baseline, B is the bumper with $0.5d$ height, C is the jet hole with compound slopes, and D is the rectangular slot. The intension of the shapes B and D is to trip the emerging cold jet. The purpose of all these geometries is to reduce the lift-off effect of the cold jet by a tripping mechanism so that it attaches to the surface downstream of the hole. The bump is introduced to trip the cold flow in a direct fashion. Such configurations may be used in conjunction with the other two concepts described above.

III. ELECTRIC FORCE MODEL

The complex dynamic nature of the film cooling flow makes it necessary to actively control it with a dynamic force that varies temporally and spatially working with the dominant turbulence scales. Both pulsed dc and ac powered plasma actuators can induce such active control over the dynamics of film cooling.

The induced force in such actuators is local (within a few millimeters) and diminishes quickly outside the domain of influence as shown in Fig. 4 schematic below. The actuator can be of the form as shown in Fig. 3(a) where the powered and grounded electrodes are kept at a sequence to push the fluid in the forward direction. A dc or ac voltage of several hundreds of volts may be applied to the powered electrode costing a few hundred watts per meter of the turbine blade. Such configurations are based on documented numerical experience and experimental evidence.[20–22] The momentum transfer between the plasma and gas happens due to collisional momentum transfer between charged ions and neutral atoms. High freestream gas temperature will enhance dissociation and hence help plasma generation due to ionization in the vicinity of the electrodes. Such actuation of the flow is active and near instantaneous, does not require any mechanical parts, and the actuator electrode sets can be applied as a patch on the surface of the existing ceramic coating of the turbine blade or embedded into the coating. There could be practical considerations such as surface oxidation of the electrodes and spallation. These need to be investigated during *in situ* testing and out of the scope for the present paper. We approximated the force as an exponentially decaying distribution with its peak just downstream of the cooling hole exit. While in practical situation this force will be transient, we consider the time average of the electric force as

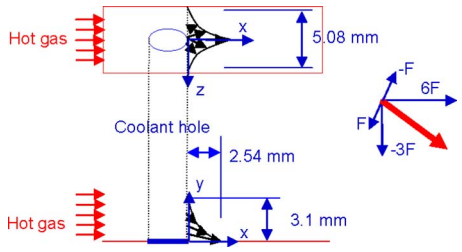

FIG. 5. (Color online) Directional distribution of the force density.

body force in our simulation. This is allowable due to largely disparate timescales of plasma and gas flow.

IV. NUMERICAL METHOD

A. Boundary conditions

Figure 1 describes schematic control volume of hot air passing over a flat surface (e.g., a turbine blade). This surface of study has a row of injection holes through which the cool air is issued at an angle $\alpha=35°$. The cool jet at temperature $T_j=150$ K is injected into the hot freestream of $T_{fs}=300$ K. The injection ducts are circular pipes with diameter equal to $d=2.54$ mm. The injection hole formed by the intersection of the injection pipe with the wind tunnel is an ellipse with the minor and the major axes d and $D=d/(\sin\alpha)$, respectively. The distance between the hole centers is $L=3d$. The selected mean flow velocities, static pressures, and temperatures (i.e., densities) in the injection pipe and the wind tunnel give a blowing ratio $M=1$. The inlet section is located at $x=-20d$ and the exit at $x=29d$. The other dimensions and boundary conditions are shown in Fig. 1. The flat (blade) surface is considered adiabatic.

At the freestream inlet $x=-20d$, an injected mass flow rate inlet condition was applied with the density ratio of $\rho_j/\rho_f=2$, velocity ratio of $u_j/u_f=0.5$, and turbulent intensity of 5%. At the exit plane $x=29d$, the gauge pressure at the outlet boundary is maintained at 0 Pa. The work surface is an adiabatic wall with a single row of holes through which cool air at temperature equal to $T_j=150$ K is injected at an angle of $\alpha=35°$ into the hot freestream of temperature $T_{fs}=300$ K. The domain extends from the plenum base at $y=-6d$ to $y=20d$ from work surface where a pressure-far-field boundary condition was applied. The periodic boundary condition was applied in the crosswise direction (at $z=\pm 1.5d$) in the computational domain. For the coolant plenum, we applied no-slip wall condition on $x/d=-14$ and 8 and $y/d=-2$ surfaces, periodic boundary condition on $z/d=-1.5$ and 1.5, and mass flow inlet condition for $y/d=-6$.

At the walls, an adiabatic wall boundary condition with no slip was imposed. All other boundaries except for the CP are maintained at homogeneous Neumann condition. The CP which is located just downstream of the coolant hole is used to actuate the flow in the following manner. The base case and the concept 1 simulation are done with CP as adiabatic wall. For concept 1, we impose the time averaged force vector shown in Fig. 5. A force approximation is recently presented for two-dimensional asymmetric actuator

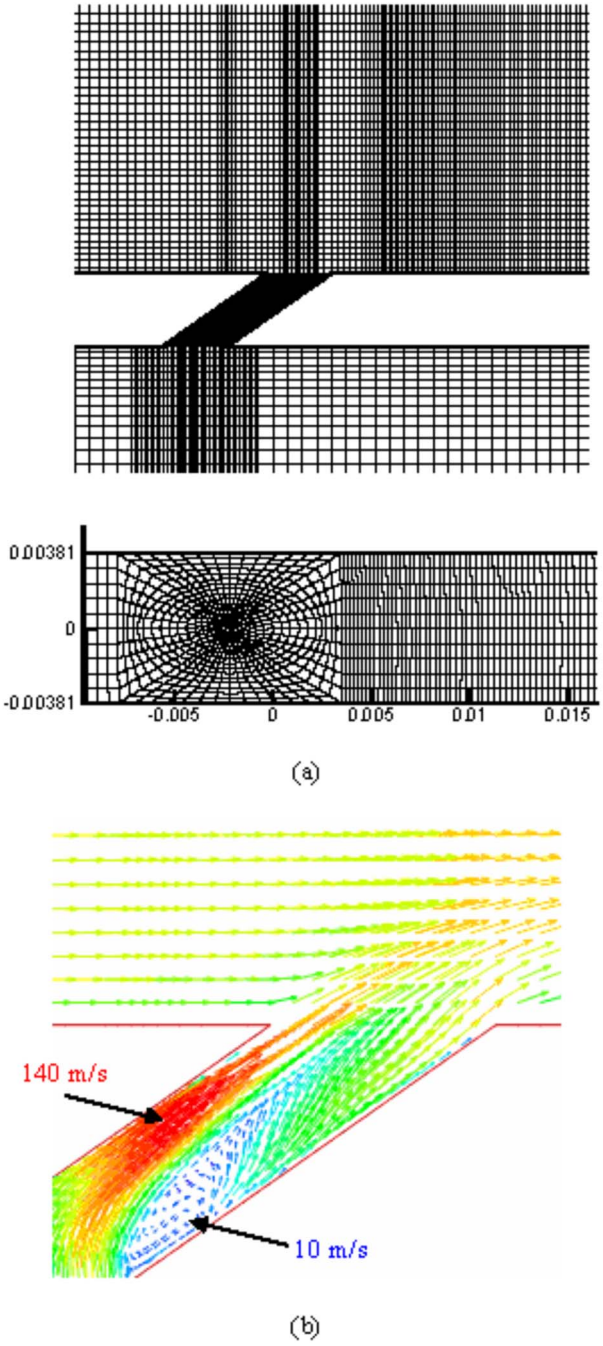

FIG. 6. (Color online) (a) Computational mesh details. (b) Steady solution of the cooling pipe shows velocity vectors (red=140 m/s and blue =10 m/s) colored by fluid speed at the central ($z=0$) plane.

configuration.[23] Here, the actuator force density is represented by a slightly modified version as $\mathbf{F}=+6F\hat{i}-3F\hat{j}\pm F\hat{k}$, where $F=L^*f_x^*f_y^*f_z$ with

$$f_x=[(x-d/2)^2+C_1]/C_2,$$

$$f_y=[\exp(-1000y)/C_3]-C_4,$$

$$f_z=[(z-d/2)^2+C_5]/C_6.$$

Λ is varied from 0 to 10 000 kN/m^3 with an increment of 2000 kN/m^3 and $C_1=1.5\times10^{-6}$, $C_2=3.09\times10^{-6}$, $C_3=0.98$, $C_4=0.057$, $C_5=1.58\times10^{-6}$, and $C_6=3.14\times10^{-6}$. For con-

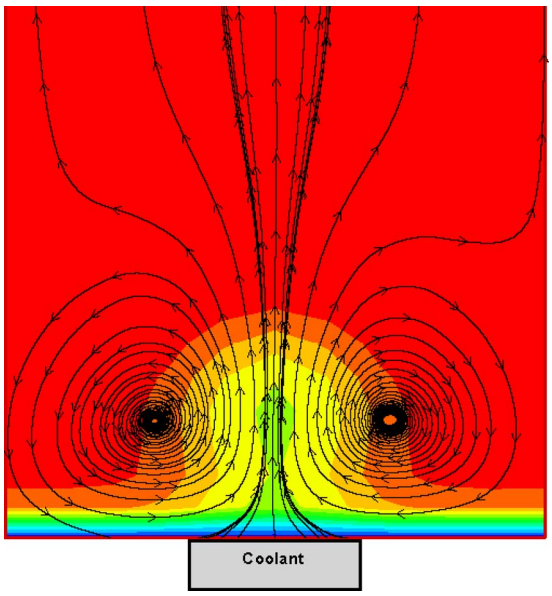

FIG. 7. (Color online) Velocity vectors at $x/d=5$ shows the well-known kidney shape flow structures.

cept 2, the CP is maintained at negative pressure $\Delta P_{CP}=P_f-P_{cp}=2823$, 3376, and 4438 Pa for three cases simulated to impose a suction condition, where P_f is freestream inlet pressure.

Depending on the actuation device, a local kN/m^3 force density may be obtained by spending a few watts.[16,21] For example, 4 mN force was measured by Gregory *et al.*[16] in a few millimeters wide actuator that consumed 20 W of power. In the current application, force density is employed in a few millimeter range. For such force density, we need around a few hundred watts to achieve it. Application of directed plasma for film cooling may require hundreds of watts to be applied per meter length of the actuator. While dielectric barrier discharge actuators may not be sufficient for this augmentation, local high-frequency (kilohertz) corona discharge may be a possible solution.

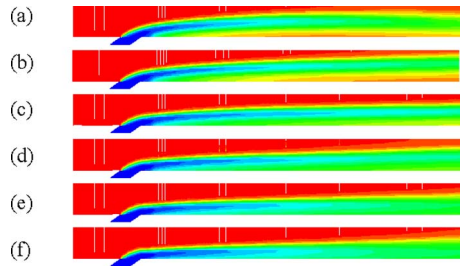

FIG. 9. (Color online) Temperature profile (red=300 K and blue=150 K) along the vertical plane at z=0 plane for Λ=(a) 0, (b) 2000, (c) 4000, (d) 6000, (e) 8000, and (f) 10 000 kN/m^3.

B. Grid information and computational approach

Using the above reduced order plasma force model, the 3D fluid description was solved by a commercial Computational Fluid Dynamics (CFD) package, FLUENT 6.3.26, based on the finite volume method. According to the experiments, the flow is compressible and turbulent. The Reynolds number based on hole diameter and inlet conditions was 16 100. A maximum Mach number not exceeding 0.3 was achieved in the flow field while maintaining the desired Reynolds number by scaling the experimental geometry down by a factor of 5. This resulted in a hole diameter of 2.54 mm, and was done to allow more rapid convergence of the solution using the density-based formulation of the computer code while minimizing compressibility effects.

We used ideal gas approximation and the Advection Upstream Splitting Method (AUSM) solver closed with Renormalized group (RNG) k-epsilon turbulence model with standard wall function.[24] We have also tried nonequilibrium wall function which resulted in very similar result. The Courant number was set equal to 1 for solution control. A second-order upwind discretization method is used. Convergence is determined when the residual among the continuity, momentum, energy, turbulent kinetic energy, and turbulent dissipation are less than 10^{-3}. Figure 6(a) shows the density of

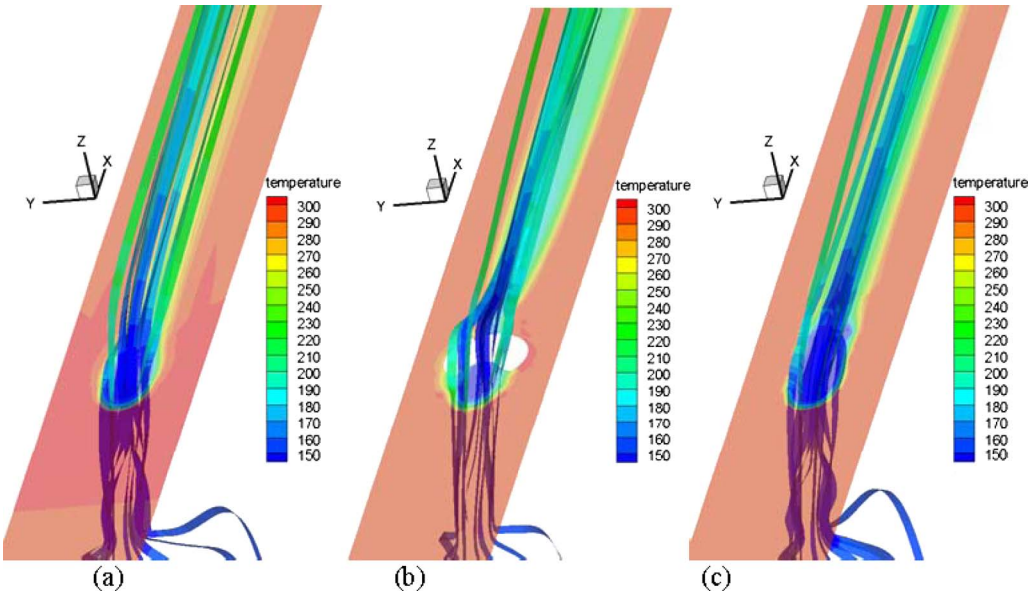

FIG. 8. (Color online) The effect of plasma actuation on trajectories of cold jet particles: (a) baseline A with $\Lambda=0$, (b) shape B with $\Lambda=2000$ kN/m^3, and (c) shape D with $\Lambda=2000$ kN/m^3.

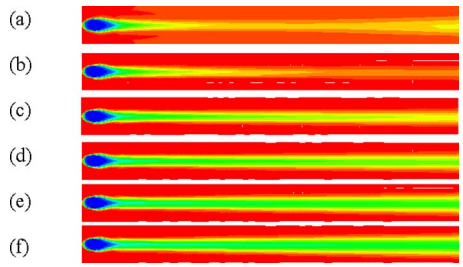

FIG. 10. (Color online) Temperature contour on the work surface ($y=0$) shows cooling flow attachment as actuation body force density increases with Λ=(a) 0, (b) 2000, (c) 4000, (d) 6000, (e) 8000, and (f) 10 000 kN/m^3.

computational grid near the coolant hole. Based on the grid independence study reported in Fig. 7 of Ref. 24, we selected approximately 200×10^3 cells for less computational cost. The base case took 1300 iterations for convergence. The base solutions are compared and are determined to be quite similar.

V. RESULTS AND DISCUSSION

12 cases were simulated for this paper. One base case, five of them relate to concept 1, three cases for concept 2, and the last three cases are for concept 3. Since we used an inherently time averaged turbulence model, computed results are presented at steady state. In Fig. 6(b), representative velocity vectors colored by speed inside the injection pipe describe a stratification of kinetic energy inside the tube. At steady state the RNG solution shows that most of the fluid is impinging at a high velocity (about 114 m/s) on the left half of the tube. Near the bottom, the entrained fluid is creating a large recirculation stretching toward the middle of the pipe. As a result, at the exit plane of the tube the flow is highly nonuniform. This is in agreement with the qualitative results reported in the literature.[2,25] Clearly, for this moderate blowing ratio $M=1$ and a combination of flow profiles at the wind tunnel and cold jet inlet, the effect of the vorticity in the pipe is not negligible. This is due to the fact that at this range of velocities existing in the pipe, the boundary layers are not

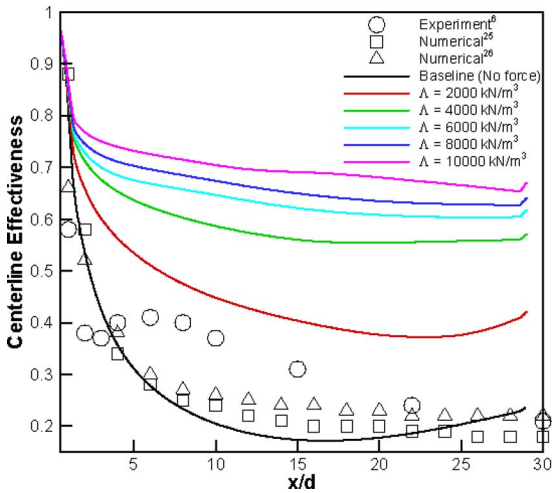

FIG. 11. (Color online) Effect of actuator force density shows significant increase in centerline effectiveness (η_c).

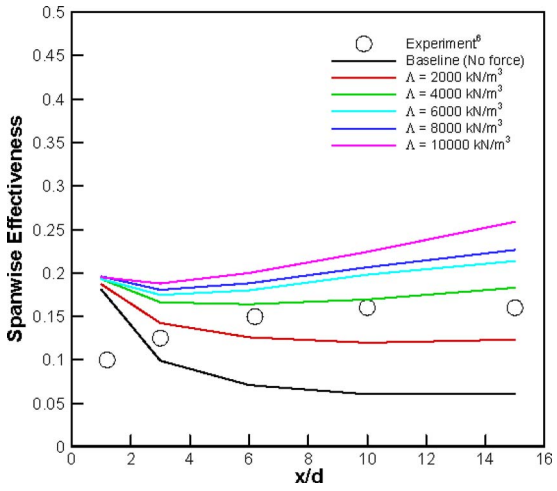

FIG. 12. (Color online) Effect of actuator force density shows significant increase in spanwise effectiveness (η_s).

thin everywhere in the pipe. It is well known that coarse grids cannot resolve the effect of the downstream vortices.

Corresponding flow field velocity vector distribution in the spanwise direction is shown in Fig. 7 at $x=5d$. The results look similar to that reported by many other researchers. The effect of the wind tunnel vorticity is significant at this plane. This is more pronounced in the u- and v-velocity profiles. The assumption of uniform velocity profile in the wind tunnel leads to higher v-values in the near wall-jet flow region. In this case, the maximum in the u-velocities is located below the maximum in the case of developed inlet profile in the wind tunnel. The tendency is that as the boundary layer in the wind tunnel becomes thicker, the velocity maxima appear at higher distances from the wall and the near wall flow changes dramatically. At very thick boundary layers, the flow close to the wall behaves as a typical boundary layer, while for very thin incoming boundary layers a wall-jet flow exists downstream the jet exit. Such flow motion creates a bound kidney shaped vortical structure that stretches downstream along the primary flow direction. Details of such structure are available in our previous publication.[1,2]

Figures 8–12 describe the effect of the imposed (plasma actuator) body force density on film cooling. Figure 8 plots the trajectories of individual cold fluid particles for the design A without any influence of plasma, and with $\Lambda=2000$ for designs B and D. It is worth noticing that downstream of the hole the fluid trips outward (crosswise) and downward in B as compared to A, while in D the cooling jet essentially clings to the work surface. The typical single counter-

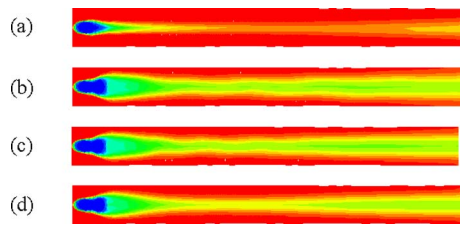

FIG. 13. (Color online) Steady state temperature contours on the plate at $y=0$ for $M=1$ (a) shows clear lift-off of the cold jet without suction. ΔP_{CP}=(b) 2823, (c) 3376, and (d) 4438 Pa.

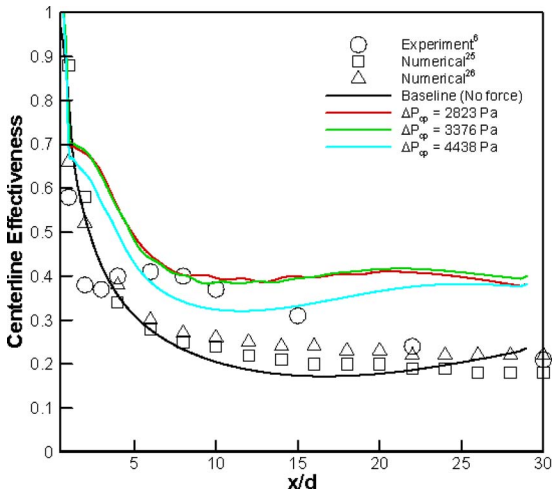

FIG. 14. (Color online) Effect of suction shows significant increase in centerline effectiveness (η_c).

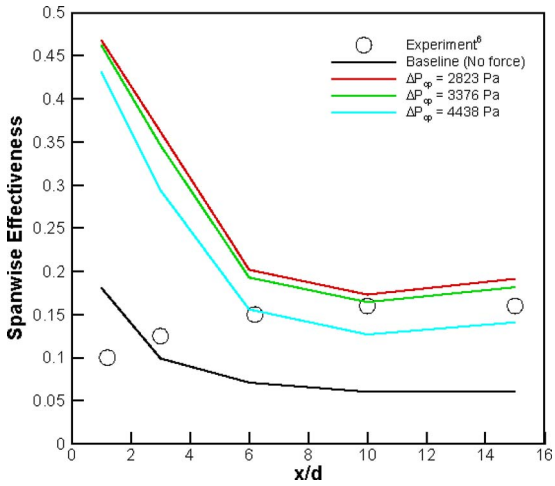

FIG. 15. (Color online) Effect of suction shows significant increase in spanwise effectiveness (η_s).

rotating vortex pair in the baseline solution for A has a peak strength of about 20 000/s as cooling jet juts out. The weaker vortices move outward and away from the wall. For design B without plasma, the strength of vortex pair doubles to 40 000/s with a much larger core diameter. Application of plasma ($\Lambda=2000$) for B splits this single vortex pair into two separate counter-rotating vortex pairs with equal strength. For design D with plasma, the single vortex pair has slightly lower strength (~35 000/s) with strong attachment toward the work surface inducing large dispersion of the cold jet. We infer that surface heat transfer may not only be improved by plasma force but also be further enhanced by local tripping of the jet as it emanates from the hole.

Figure 9 plots the temperature distribution on the vertical midplane ($z=0$). It is easy to see from the temperature distribution how the lift-off causes significant reduction in cooling effectiveness. As we increase the body force density from an initial zero ($\Lambda=0$, no actuator) to a maximum of $\Lambda=10\,000$ kN/m^3 (effective force ~N), the flow completely attaches to work surface. Note that this could be done actively either by embedded sensing of the blowing ratio or, even better, the mean effectiveness on the work surface. Figure 10 shows the temperature distribution on the horizontal work surface ($y=0$). Importantly, the actuation force applied in a 3D manner demonstrates successful spreading of the cold film over the flat (blade) surface not only in the streamwise direction but also in the crosswise fashion. Thus the cooling performance should reflect such improvement.

Figure 11 plots the centerline effectiveness (η_c) while Fig. 12 shows the spanwise averaged effectiveness (η_s) over the work surface. The computed centerline results for the base case (no control) compare reasonably with the experiment of Sinha *et al.*[6] and two other previously reported numerical results.[26,27] At $x/d=5$ the effect of plasma actuation is evident. Figure 11 shows that η_c increases by over 100% as the force density increases to the maximum. Figure 12 shows that η_s also improves demonstrating the 3D flow control. Interestingly, this η_s keeps on increasing with distance from the cooling hole. For example, at $x/d=1$, the effective increases from 0.18 to 0.2 as Λ varies from 0 to 10 000 kN/m^3, at $x/d=6$, it increases from 0.07 to 0.19, and

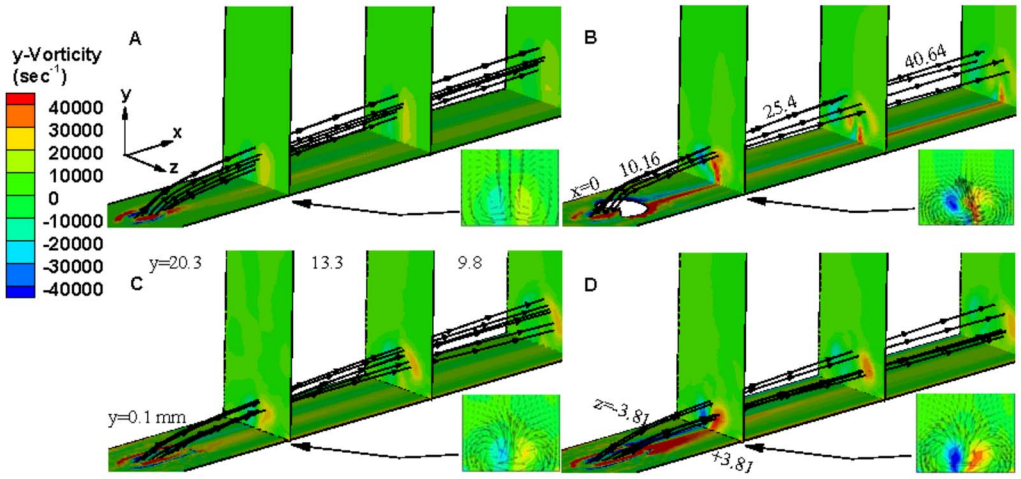

FIG. 16. (Color online) Velocity vectors and contours colored by the y-vorticity at $x/d=4$, 10, and 16. The inset hole schematics show various shapes for designs A–D.

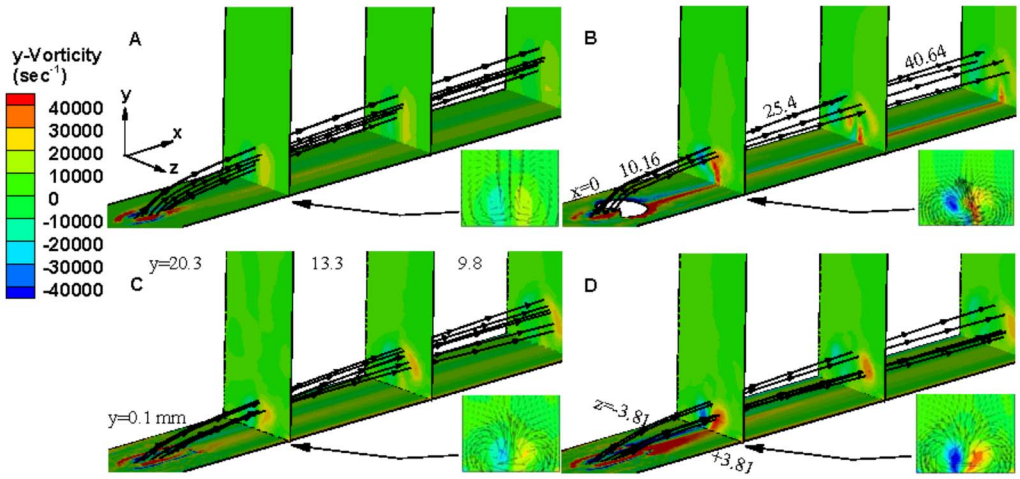

FIG. 17. (Color online) Velocity vectors and contours colored by the y-vorticity at $x/d=4$, 10, and 16 for designs A–D with actuation force density $\Lambda=2000\ \mathrm{kN/m^3}$.

at $x/d=15$, it increases from 0.06 to 0.22 (by over 250%). Such increase confirms the active influence of plasma actuator in enhancing the film cooling.

Figures 13–15 plot the effect of suction hole placed in the CP region. The suction hole ends at $x/d=1$. Computed temperature distribution along the work surface is shown. Figure 13 shows how the jet lift-off diminishing the cooling performance at blowing ratio of $M=1.0$. The attachment and hence the cooling effectiveness is further increased by using a small suction of $\Delta P_{\mathrm{CP}}=2823$, 3376, and 4438 Pa, respectively. Interestingly, ΔP_{CP} of 2823 and 3376 Pa works better than the case of 4438 Pa. Figure 14 shows a good improvement of centerline effectiveness (η_c) by 50% at $x/d=5$. The jet attaches completely just downstream of the cooling hole increasing η_c drastically by 260% (from 0.1 to 0.36) at $x/d=3$ in Fig. 15. Even though the cool jet does not remain attached further downstream, the cooling performance increases from 0.06 to 0.2 at $x/d=15$ for $\Delta P_{\mathrm{CP}}=2823$ Pa.

Figure 16 shows the evolution of the vortices from $x/d=4$ to 16 and presents y-vorticity contours with velocity vector overlays at $x/d=4$ for hole shapes A, B, C, and D. The baseline solution for design A shows the typical counter-rotating vortex pair with peak vortex strength of about 20 000/s as cooling jet juts out. We can see the weaker vortices are moving outward and away from the wall as the distance increases. For design B, the strength of vortex pair doubles to 40 000/s with a much larger core diameter. This is due to the tripping of cold jet over the bump. The peak vorticity is a few millimeters above the work surface. Design C shows slightly higher (25 000/s) vorticity than that of A, but this value is substantially lower than that of B or D. In later design the peak is about the same as that of B, however, it is attached to the work surface allowing significantly higher horizontal dispersion of the cooling jet. Figure 17 plots the effect of strong downward and forward forces for $\Lambda=2000\ \mathrm{kN/m^3}$. For design A, the y-vorticity is lower than that in Fig. 16 without plasma effect because the electric force slightly kills the strength of the vortex. Clearly, for designs B–D, the counter-rotating vortex pairs change their direction from an outward swirl to an inward swirl because the downward momentum induced by the electric force is much larger than the upward momentum of the cooling jet. For design B, the single vortex pair of Fig. 17 splits into two separate vortex pairs with equal strength, while for designs C

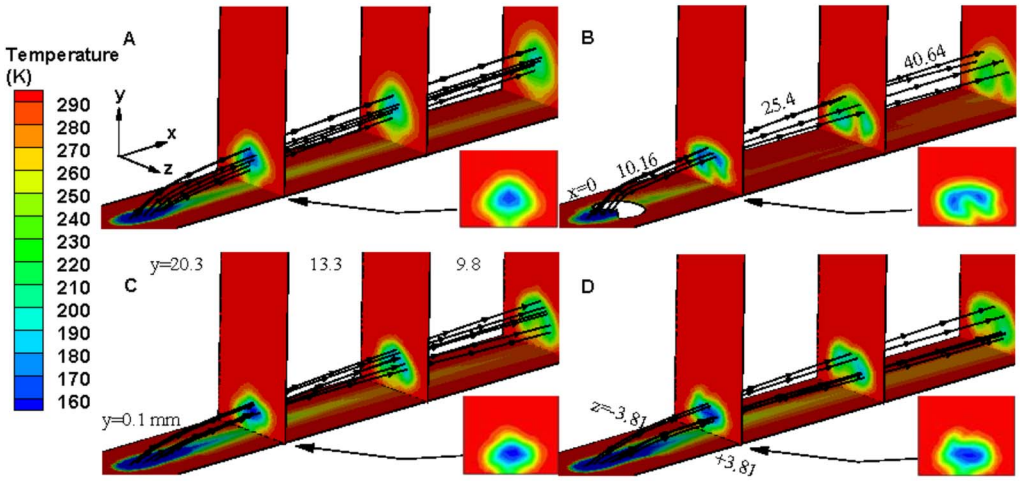

FIG. 18. (Color online) Temperature contours at spanwise plane ($x/d=4$, 10, and 16) for various designs A–D.

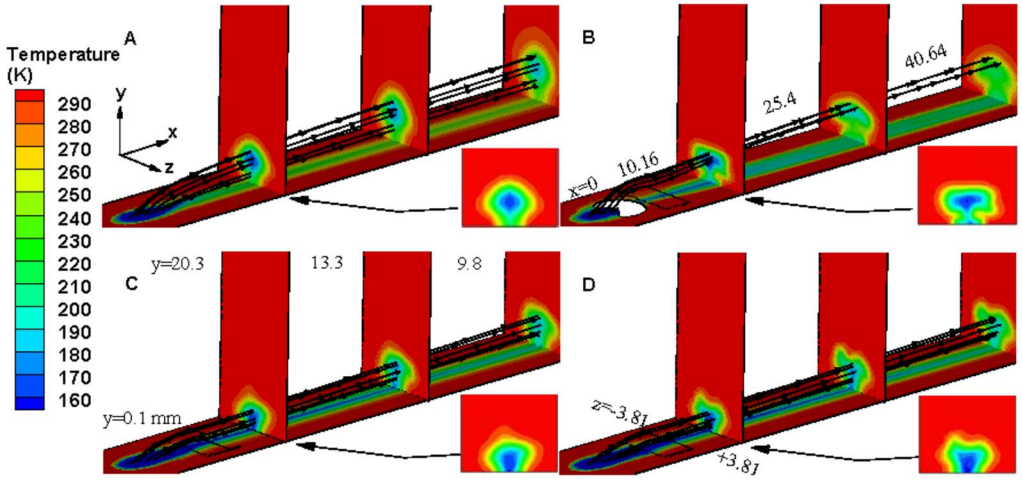

FIG. 19. (Color online) Temperature contours at spanwise plane ($x/d=4$, 10, and 16) for designs A–D with actuation force density $\Lambda=2000$ kN/m^3.

and D the single vortex pair with slightly lower strength (~35 000/s) shows strong attachment toward the work surface inducing large dispersion of the cold jet. Application of plasma discharge changes the near wall dynamics of flow which is also reflected in heat transfer.

Figure 18 plots the temperature distribution on the same planar location ($x/d=4$, 10, and 16) and marks y-z plane temperature distribution at $x/d=4$ for no actuation $\Lambda=0$. At this distance, the cold fluid lifts off in traditional design A. As the distance increases at $x/d=16$ for design A, the lift-off effect becomes aggravated. The situation worsens for B just beyond the bump. However, for C and D the cold jet bends (trips) for modest improvement of the cooling region on the work surface. In contrast, the influence of plasma induced electric force can be significant as seen in Fig. 19 for $\Lambda=2000$ kN/m^3. The temperature of the work surface reduced for all designs. For design A at $x/d=16$, the lowest temperature 230 K on the work surface is much cooler than that in Fig. 18 for the same design and location. Clearly (in designs for B, C, and D), the cold jet attaches to the work surface, the extent of which increases from B to C to D. It is thus essential to quantify the improvement in cooling performance.

Figure 20 plots the effect of plasma actuation on centerline effectiveness (η_c) for the four designs A–D. Figure 20(a) shows the effect of geometric modifications ($\Lambda=0$) of the cooling hole. The performance plots of different hole shapes show that C and D have better η_c before $x/d=6$ because the expansion of the jet reduces the momentum ratio increasing the cooling performance. Also the step at the edge of D acts as a trip for the cold fluid inducing more attachment. Interestingly, case B provides higher η_c beyond $x/d=20$ because the jump effect delays the cold fluid attached to the work surface. The η_c in Fig. 20(b) increases by over 70%, 558%, 137%, and 164%, respectively, at $x/d=5$ than in Fig. 20(a) as the force density increases to the maximum ($\Lambda=2000$) for designs A–D. Figure 21 shows the spanwise averaged effectiveness (η_s) for the four designs A–D. Figure 21(a) shows that the baseline design A has better η_s than that of B because the jump effect causes the counter-rotating vortex pair moving away from the wall. Designs C and D have good improvement over 70% in η_s at $x/d=3$ because the slot design reduces the momentum of the cooling jet and gives more chances to cool the wall near the cooling hole. Figure 21(b) shows the plasma effect of designs A–D as force den-

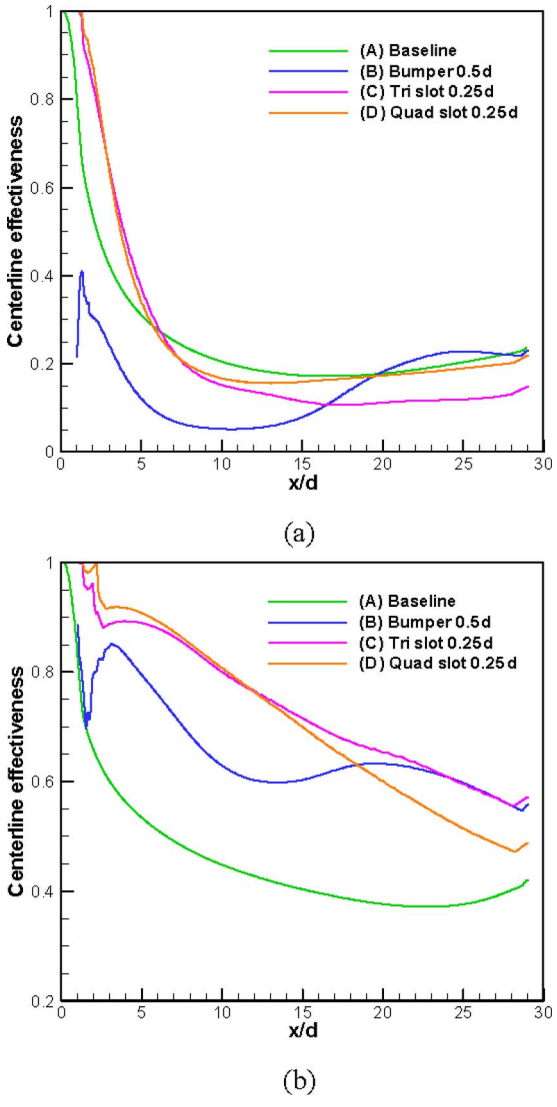

FIG. 20. (Color online) Effect of plasma actuation on centerline effectiveness (η_c) for (a) $\Lambda=0$ and (b) $\Lambda=2000$ kN/m^3.

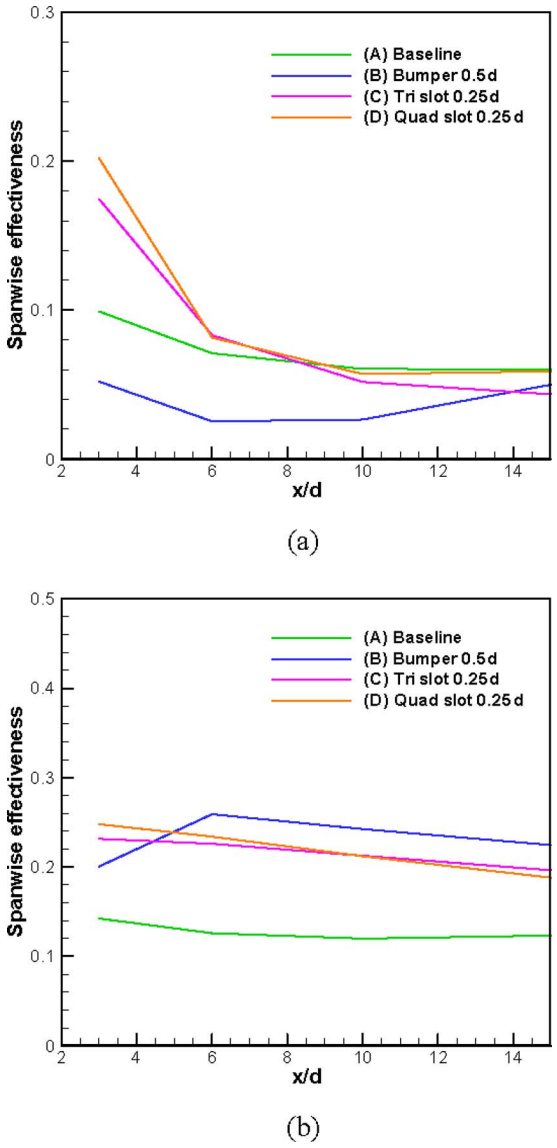

FIG. 21. (Color online) Effect of plasma actuation on spanwise effectiveness (η_s) for (a) $\Lambda=0$ and (b) $\Lambda=2000$ kN/m^3.

sity increases to the maximum ($\Lambda=2000$). Evidently plasma actuation gives a very good improvement for designs B–D. It is evident that the plasma flow control guarantees that the flow is attached to the surface improving the heat transfer drastically.

VI. CONCLUSION

Three concepts are introduced for improved film cooling. Concept 1 using plasma actuator, concept 2 using suction just downstream of the cooling hole, and concept 3 using various hole shapes with plasma actuation show significant enhancement in streamwise and lateral cooling, improving the effectiveness by over 100%. In the near field region, the suction method works better for improving cooling performance while plasma actuator induced body force works uniformly well along the entire blade surface. The bumper design B did not appear as a good choice as compared to the configurations C and D to cool the surface near downstream of the hole. Application of plasma, however, remedies that shortfall. Despite some limitations of suction, the possible benefit of internal cooling may be realized by a conjugate analysis. This could be a topic for further study. Also hybrid DES- and/or LES-type turbulence model will possibly be better to capture such complex flow structures. Such effort will take much longer simulation time and may be another topic for a follow-on study. Realistic experimentation is underway to validate these designs. Plasma augmented design modified flow control ideas may become more beneficial for cases with badly separated jets at higher velocity ratio. This remains to be tested.

[1]S. Roy, Numer. Heat Transfer, Part A **38**, 701 (2000).
[2]S. Kapadia, S. Roy, and J. Heidmann, J. Thermophys. Heat Transfer **18**, 154 (2004).
[3]D. G. Hyams and J. H. Leylek, J. Turbomach. **122**, 122 (2000).
[4]S. V. Ekkad, S. Ou, and R. B. Rivir, J. Turbomach. **128**, 564 (2006).
[5]H. Kruse, *Heat and Mass Transfer in Rotating Machinery (A86-24451 09-34)* (Hemisphere, Washington, DC, 1984), pp. 451–461.
[6]A. K. Sinha, D. G. Bogard, and M. E. Crawford, J. Turbomach. **113**, 442 (1991).
[7]R. S. Bunker, ASME J. Heat Transfer **127**, 441 (2005).
[8]J. H. Leylek and R. D. Zerkle, J. Turbomach. **116**, 358 (1994).
[9]R. Fearn and R. P. Weston, AIAA J. **12**, 1666 (1974).
[10]V. K. Garg and D. L. Rigby, Int. J. Heat Fluid Flow **20**, 10 (1999).
[11]J. D. Heidmann, D. L. Rigby, and A. A. Ameri, J. Turbomach. **122**, 348 (2000).
[12]V. K. Garg, Int. J. Heat Fluid Flow **21**, 134 (2000).
[13]M. Lesieur, P. Comte, E. Lamballais, O. Métais, and G. Silvestrini, J. Eng. Math. **32**, 195 (1997).
[14]M. Strelets, AIAA Paper No. 01-0879, 2001.
[15]C. M. Ho and P. Huerre, Annu. Rev. Fluid Mech. **16**, 365 (1984); B. A. Haven and M. Kurosaka, J. Fluid Mech. **352**, 27 (1997).
[16]J. W. Gregory, C. L. Enloe, G. I. Font, and T. E. McLaughlin, 45th AIAA Aerospace Sciences Meeting and Exhibit, Reno, NV, 2007 (unpublished), Paper No. AIAA-2007-185; D. V. Roupassov, A. A. Nikipelov, M. M. Nudnova, A. Yu. Starikovskii, 44th AIAA/ASME/SAE/ASEE Joint Propulsion Conference & Exhibit, Hartford, CT, 2008 (unpublished), Paper No. AIAA-2008-5607.
[17]J. L. Levengood and T. A. Auxier, U.S. Patent No. 4753575 (1988).
[18]F. O. Soechting and T. A. Auxier, U.S. Patent No. 6129515 (2000).
[19]A. Riahi, R. McDonald, and F. G. Borns, U.S. Patent No. 7223072 (2004).
[20]S. Roy, Appl. Phys. Lett. **86**, 101502 (2005).
[21]S. Roy and D. Gaitonde, Phys. Plasmas **13**, 023503 (2006); AIAA Paper No. AIAA-2007-185, 2007.
[22]A. Labergue, L. Leger, E. Moreau and G. Touchard, J. Electrost. **63**, 961 (2005).
[23]K. P. Singh and S. Roy, J. Appl. Phys. **103**, 013305 (2008).
[24]X. Z. Zhang and I. Hassan, J. Thermophys. Heat Transfer **20**, 754 (2006).
[25]J.D. Heidmann and S.D. Hunter, ASME Paper No. 2001-GT-0138, 2001.
[26]A. A. Immarigeon, M.S. thesis, Concordia University, Montreal, 2004.
[27]K. B. Mulugeta, and S. V. Patankar, ASME Paper No. 96-WA/HT-8, 1996.